Crystal structure of a fungal elicitor secreted by *Phytophthora cryptogea*, a member of a novel class of plant necrotic proteins

Guillaume Boissy[1], Eric de La Fortelle[2], Richard Kahn[3], Jean-Claude Huet[1], Gérard Bricogne[2,4], Jean-Claude Pernollet[1] and Simone Brunie[1]*

Background: Elicitins form a novel class of plant necrotic proteins which are secreted by *Phytophthora* and *Pythium fungi*, parasites of many economically important crops. These proteins induce leaf necrosis in infected plants and elicit an incompatible hypersensitive-like reaction, leading to the development of a systemic acquired resistance against a range of fungal and bacterial plant pathogens. No crystal structures of this class of protein are available. The crystal structure determination of β-cryptogein (CRY), secreted by *Phytophthora cryptogea*, was undertaken to identify structural features important for the necrotic activity of elicitins.

Results: The structure of CRY was determined using the multiwavelength anomalous diffraction technique and refined to 2.2 Å resolution. The overall structure has a novel fold consisting of six α helices and a beak-like motif, whose sequence is highly conserved within the family, composed of an antiparallel two-stranded β sheet and an Ω loop. This motif is assumed to be a major recognition site for a putative receptor and/or ligand. Two other distinct binding sites seem to be correlated to the level of necrotic activity of elicitins.

Conclusions: The determination of the crystal structure of a member of the elicitin family may make it possible to separate the activity that causes leaf necrosis from that inducing systemic acquired resistance to pathogens, making it feasible to engineer a non-toxic elicitin that only elicits plant defences. Such studies should aid the development of non-toxic agricultural pest control.

Addresses: [1]Unité de Recherche Biochimie & Structure des Protéines, INRA, 78352 Jouy-en-Josas, France, [2]MRC-LMB, Hills Road, Cambridge CB2 2QH, UK, [3]IBS, 41 Av. des Martyrs, 38027 Grenoble, Cedex 1, France and [4]L.U.R.E, Bât. 209d, 91405 Orsay Cedex, France.

*Corresponding author.
E-mail: brunie@jouy.inra.fr

Key words: elicitin, multiwavelength anomalous diffraction (MAD), plant pathogen, toxin, X-ray crystallography

Received: 2 August 1996
Revisions requested: 29 August 1996
Revisions received: 3 October 1996
Accepted: 8 October 1996

Structure 15 December 1996, 4:1429–1439

Introduction

Most microorganisms that attempt to establish themselves as parasites on plants are defeated by the defences marshalled by the prospective host during the invasion process. These defence mechanisms are stimulated by molecules of microbial origin, generically termed elicitors, which induce one or more reaction cascades, usually resulting in a necrotic hypersensitive response [1]. This may lead to the development of systemic acquired resistance in which host tissues remote from the inoculation site become resistant to attack by microorganisms, including pathogens other than the one that was responsible for the initial, unsuccessful, attack [2,3].

Among plant pathogens, the fungal genus *Phytophthora* includes many species that are parasites of a diverse range of species, including many economically important crops. With the exception of *Phytophthora parasitica var. nicotianae*, all the *Phytophthora* species studied to date in culture secrete large amounts of one or several elicitin isoforms that act as toxins in order to weaken the host [4,5]. Recently, elicitin isoforms were also observed to be secreted from an Oomycete fungus belonging to the genus *Pythium* [6]. Elicitins are a novel class of toxic protein elicitors that cause remote leaf necrosis and induce, in some plant species, systemic resistance against fungal and bacterial pathogens [2,3]. They are secreted from the pathogen in a process that includes the removal of a signal peptide, enter the plant through the root system and proceed to the leaves where they induce necrosis without requiring further biochemical alterations within this plant to be active [5].

No homology with any other protein sequence has been detected for the 12 *Phytophthora* and *Pythium* elicitins sequenced to date, but they show more than 60% sequence identity with each other. This strongly suggests that these 10 kDa proteins constitute a new family. Elicitins from different fungal species, when applied to tobacco plants at equal doses, exhibit different levels of necrotic activity, but induce protection in the plants at the same level [3]. Using these differences in necrotic activity on tobacco, the elicitin family has been classified into acidic α-elicitins and basic β-elicitins, the latter being much more necrogenic than the former. This classification is roughly independent of the ability of the elicitins to activate plant defence mechanisms. Highly necrotic β-elicitins cause visible leaf necrosis when applied at approximately 100 pmoles per plant, whereas a 50–100-fold increase in concentration is required

to elicit the same reaction using one of the weakly-necrotic α-elicitins. These differences in biological activity can be correlated with the sequence differences and the physicochemical features of elicitins [5–12]. By comparing the sequences of various elicitins and relating them to the corresponding necrotic indices in tobacco plants, it is possible to identify potential necrotic-modulating residues at positions 2, 13, 72 and 94. The nature of the sidechain of residue 13 has the most consistent correlation with severity of the necrotic effects. All the highly necrotic β-elicitins have a hydrophilic sidechain at position 13, usually a lysine, whereas the less necrotic α-elicitins have a hydrophobic valine at this position. To evaluate the contribution of residue 13 to the necrotic activity of elicitins, a recombinant elicitin has been produced in *E. coli* using a synthetic gene encoding β-cryptogein (CRY), a basic elicitin secreted by *Phytophthora cryptogea*. Replacement of lysine 13 by a valine using site-directed mutagenesis experiments led to a dramatic alteration of the toxicity of the mutated recombinant protein [13], reducing it to the toxicity level of an α-elicitin. In spite of the identification of many cellular events that occur in response to the action of elicitins in the plant, to date nothing is known about the action of elicitins at the molecular level. However, specific high affinity binding sites for CRY have been observed in the tobacco plant plasma membrane [14].

In this paper, we describe the first example of a three-dimensional structure of an elicitin. The X-ray crystal structure of wild-type CRY has been determined at 2.2 Å resolution. It reveals three distinct sites on the surface of the protein that are likely to be involved in the toxic function of elicitins. A rational approach to mutagenesis to map the functional sites of elicitins, is now possible using a gene encoding for CRY overexpressed in *Pichia pastoris* [15].

Results and discussion

Structure determination

CRY crystallizes in the space group $P4_122$ with cell dimensions a = b = 46.5 Å, c = 134.9 Å [16]. An extensive search for heavy-atom derivatives yielded only one, a poorly phasing platinum derivative. We therefore solved the crystal structure of CRY by the multiwavelength anomalous diffraction (MAD) phasing method. Four data sets were collected in the vicinity of the platinum L_{III} absorption edge (Table 1) on the D2AM beam line at the European Synchrotron Radiation facility (ESRF, Grenoble, France). As previously reported [17], a vast improvement of the phases was obtained by the introduction of a native data set. The refinement of heavy-atom parameters and the calculation of phase probability distributions were performed using the program SHARP [18]. The use of this new program was a decisive factor in obtaining an interpretable electron-density map. The data structure in SHARP allows the native dataset to be on an equal footing with those of any derivative; incorporating native measurements on top of a MAD dataset was simple and required no special procedures such as phase combination or use of negative occupancies. The extra isomorphous information introduced into the phasing process using this method was especially useful for centric reflections (27% of the data to 3.0 Å), which are devoid of anomalous signal, and also for very low-resolution reflections (below 16.5 Å) for which anomalous differences were not measured.

The electron-density was so well defined (Fig. 1a) that the atomic model could be built for the whole molecule

Table 1

Summary of data collection.

			K_2PtCl_4 derivative*			
	Native1	Native2	remote1 λ1	edge λ2	peak λ3	remote2 λ4
X-ray source	LURE	ESRF	ESRF	ESRF	ESRF	ESRF
Temperature (°)	4 C	100 K	100 K	100 K	100 K	100 K
Wavelength (Å)	0.91	1.0500	1.0766	1.0726	1.0722	1.0696
Unit cell size (a = b, c) (Å)	46.5, 134.9	46.4, 132.8	46.1, 132.3			
d_{min}‡ (Å)	2.2	2.9	2.9	2.9	2.9	2.9
Number of observations	35101	13922	19956	22323	26399	24029
Number of unique reflections	7864	3404	3074	3169	3264	3246
completeness (%)	97.2	98.2	88.0	90.3	92.6	92.4
Multiplicity	3.1	4.2	6.5	7.0	8.1	7.4
Number of unique Bijvoet pairs	-	-	2144	2208	2302	2279
$I > 3\sigma$ (%)	92.9	91.8	96.2	96.5	96.5	96.5
R_{sym}† (%)	3.2	5.9	4.8	4.9	5.0	5.0
in highest resolution shell	15.0	9.1	9.0	11.6	7.7	7.1

*The crystal was soaked in the dark for 6 h in the sitting drop where it had grown, reaching a final concentration of 50 mM K_2PtCl_4. The soaked crystal was much more sensitive to radiation damage.

†$R_{sym} = \Sigma_h \Sigma_i | I_i(h) - < I(h) > | / \Sigma_h \Sigma_i I_i(h)$, where $I_i(h)$ is the i^{th} observation of reflection h and $< I(h) >$ the average intensity obtained from the same reflection observed i times. ‡d_{min} is the minimum Bragg spacing.

Figure 1

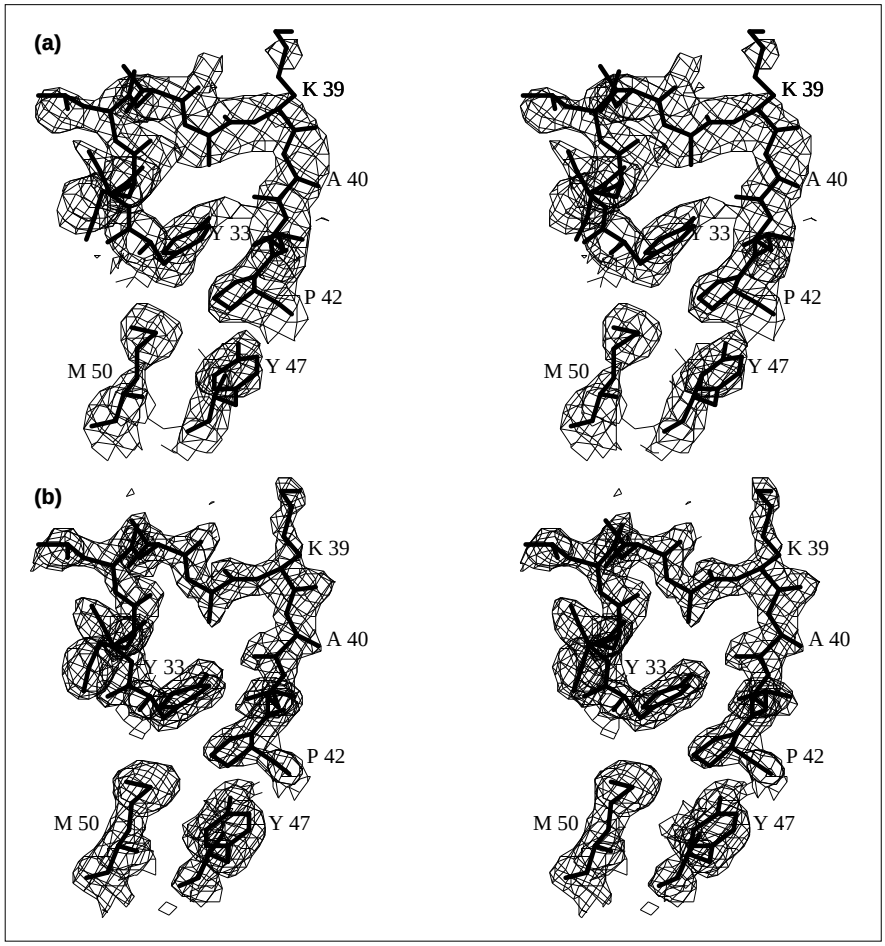

Stereoviews of the original and final electron-density maps of CRY. (a) The 'MAD+native' (original) electron-density map calculated at 3.0 Å resolution using solvent-flattened experimental phases with residues of the Ω loop of the final refined model superimposed in thick lines. (b) The $2F_o–F_c$ calculated phased map generated from the refined coordinates at 2.2 Å resolution showing the same region of the molecule as (a). Both maps are contoured at the 1.5 σ level.

without ambiguity. The refined model gave a crystallographic R factor of 21.8% for the 6987 reflections with $F > 2\sigma F$ between 7 Å and 2.2 Å. A total of 66 water molecules was included in the final model, for which the statistics are summarized in Table 2. A portion of the $2F_o–F_c$ electron-density map, calculated after completion of the refinement, is shown in Figure 1b. The Ramachandran plot [19] indicates that 97.8% of the residues are in the most favoured regions with no outlier residues in the disallowed region. Only two residues are in the 'generously allowed' region, and both are well defined by the electron-density.

Overall structure

CRY is a globular protein of approximate dimensions 39×26×25 Å. The details of the extent of the secondary structure are given in Figures 2 and 3. The fold is mainly α-helical, comprising six α helices (α1–α6). In agreement with results from circular dichroism experiments [8], α helices account for 56% of the structure. All the helices are concentrated on one face of the molecule, strengthening the tertiary structure acting as a belt. In contrast, the other face of the molecule has an unusual shape, with two protruding loops; one is an Ω loop and the other contains a β sheet. The overall fold of CRY shows no resemblance to any reported protein topology. Indeed, a search using the programs DALI [20], DEJAVU [21] and VAST [22], which allow a systematic search for homologous three-dimensional structural motifs in the Brookhaven Protein Data Bank [23], revealed no similar topology.

The common core

The tertiary structure of CRY is rigidly held in place by three disulfide bridges. Corresponding disulfide bridges have previously been established for the α-elicitin secreted by *Phytophthora capsici* by NMR studies [24]. In CRY, Cys3–Cys71 links the N-terminal polypeptide to the β sheet, Cys27–Cys56 joins helices α2 and α4, and Cys51–Cys95 maintains position of the C-terminal helix α6 relative to helix α3. In addition, a salt bridge (Asp21–Lys62) binds the short connecting loop between helices α1 and α2 to helix α4. The hydrophobic core of the molecule is mainly occupied by a cluster of three methionines, Met35, Met50 and

Table 2

Summary of refinement statistics of final model with 4°C native data (Native1).

Refinement data	
Resolution range (Å)	7.0–2.2
No of reflections	
Total	7583
Used for refinement ($\sigma_{cut\text{-}off} = 2$)	6987
R_{free} calculation	596
No of non hydrogen atoms	
Protein	717
Water	66
Validity of the model	
R factor* (%)	21.8
R_{free}† (%)	27.9
Average temperature factors (Å^2)	
Mainchain	35.8
Sidechains	37.1
Solvent molecules	47.2
Rms deviations from ideality	
Bond lengths (Å)	0.013
Bond angles (°)	1.50
Ramachandran plot [19]	
Residues in most favoured regions (%)	97.8
Residues in additional allowed regions (%)	2.2
Overall G factor‡	0.02

*R factor = $\Sigma||F_{obs}| - |F_{calc}|| / \Sigma|F_{obs}|$, where F_{obs} and F_{calc} are the observed and calculated structure factor amplitudes. A small fraction (7.5 %) of reflections were randomly selected and used to calculate the †R_{free}. ‡G factor is the overall measure of structure quality from PROCHECK [45].

Met59, the disulfide bridge Cys27–Cys56, the sidechains of Ile60 and Ile63 and the aromatic rings of Tyr87 and Phe91. The three disulfide bonds, the salt bridge and the 39 amino acids that define this hydrophobic core are invariant in the known *Phytophthora* elicitins. Therefore one can expect that all the members of the elicitin family will share a very similar tertiary structure.

The beak-like motif

The loop from Tyr33 to Pro42 is an Ω loop, the distance between the two Cα (6.9 Å) being in the range defined by Leszczynski and Rose [25]. Although only a few electrostatic interactions stabilize the Ω loop, its conformation is surprisingly well defined and is shaped according to the position of the cumbersome, hydrophobic, phenolic ring of the invariant Tyr33. This Ω loop was already well defined in the initial 'MAD+native' electron-density map (Fig. 1a). The hydroxyl atom of Tyr33 interacts with the carbonyl oxygen of Ala40, and due to the presence of a reverse turn between Met35 and Thr37, the carbonyl oxygen of Ser34 is hydrogen bonded to the backbone nitrogen of Ala38. In addition, the stacking of the sidechains of Tyr33, Pro42 and Tyr47 enhances the rigidity of the whole loop. The loop created by the antiparallel two-stranded β sheet (β1–β2) connects the two helices α4 and α5 and contains a reverse turn from Pro76 to Ser78. The Ω loop and the β sheet are interestingly shaped in a beak-like arrangement, with the two reverse turns facing each other. We have dubbed this structural feature the beak-like motif. It is remarkable that this motif is essentially made of residues that are invariant in the elicitin family, with most of the variable residues belonging to the helices on the opposite face of the molecule (Fig. 2a). Studies on Ω loops have shown that they are often important for protein function and stability [26]. In the CRY structure, it is clear that the conserved beak-like motif is essential for the structural stability and folding of the protein. However, the interaction between the Ω loop and β sheet is weak as only two hydrogen bonds are involved in their contact (Thr77Oγ and Ser78Oγ are respectively hydrogen bonded to the carbonyl oxygens of Leu36 and Ala38).

Proposed binding sites

Given the unusual biological properties of the elicitins, induction of plant-cell necrosis and plant systemic resistance to an array of pathogens, it seems clear that the elicitin proteins must interact with one or more plant receptors. A receptor-like binding factor on the tobacco plant plasma membrane is one of the possible candidates for a CRY receptor, as suggested by Wendehenne *et al.* [14]. The Ω loop and the β sheet both exhibit stable conformations, a feature which should be common to all of the elicitins because of their high degree of sequence identity. It is tempting to imagine that the conserved structural beak-like motif may be important in protein function. As the interaction between the Ω loop and β sheet is weak, when the protein interacts with a receptor and/or a ligand, it seems plausible that the beak-like motif may open; the Ω loop might act as a hinge upon binding. If so, this motif might be a major site for receptor/ligand recognition and an important element in the function of protein.

As previously noted [14], binding seen to plasma membrane receptors may be abrogated out by the modified charge density induced by changes on either the pH on the ionic strength of the solution in which the experiment is performed. This observation might explain the fact that acidic α-elicitins and basic β-elicitins show clearly distinct levels of toxicity. There are few variable amino acids of the elicitin family, four of which (in position 2, 13, 72 and 94) seem to be correlated to the level of toxicity of the proteins (Fig. 4). Residue 13, which is lysine in highly necrotic β-elicitins and valine in the less necrotic α-elicitins, seems to be particularly important in determining the level of toxicity [13]. In the CRY structure, Lys13 lies in the middle of helix α1, well exposed to the solvent, in a region mainly composed of variable residues. The charge distribution of the electrostatic potential calculated on the solvent-accessible surface, (Fig. 5), highlights distinct patches of positive,

Figure 2

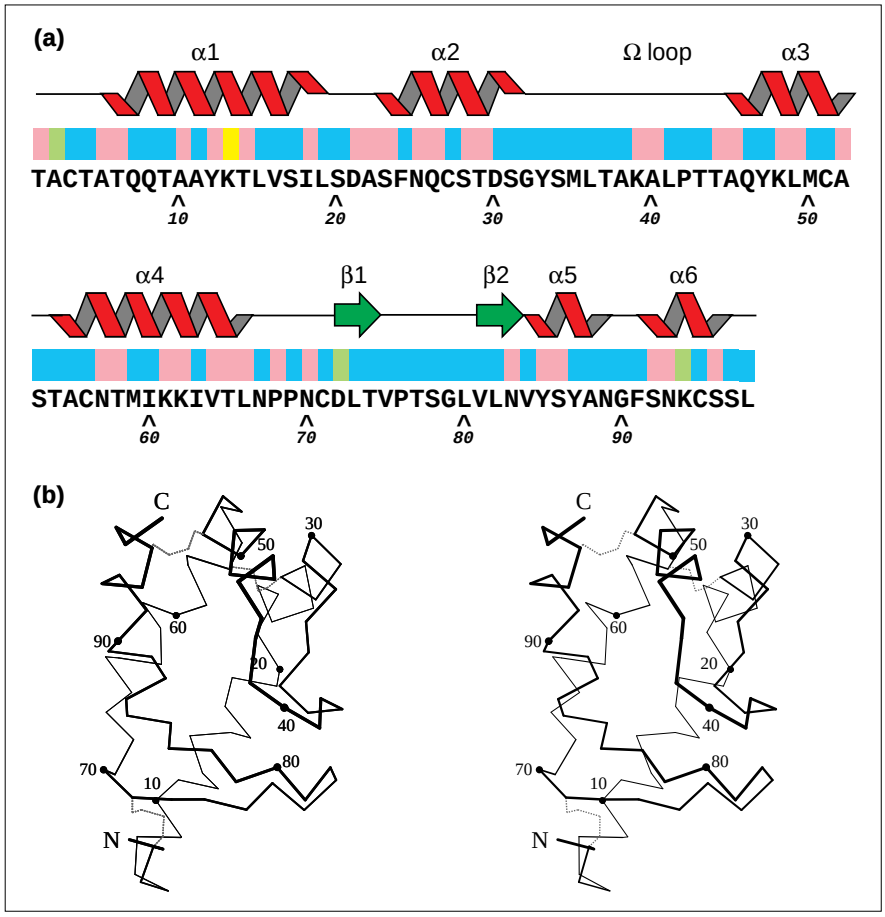

The secondary structure of CRY. (a) The secondary structure elements, assigned by PROCHECK [45], are aligned with the sequence of CRY. Coloring scheme is derived from the alignment of 12 sequences of elicitins [5–12]. Invariant residues are shown in blue and variable residues in pink. Two stretches of invariant residues are located on the Ω loop and the antiparallel two-stranded β sheet (β1–β2). The toxicity-related residue 13 is indicated in yellow and the three residues (2, 72 and 94) likely to be correlated to the level of toxicity are colored in green. (b) A stereo view of the Cα trace of CRY with every tenth residue numbered and the N and C termini are labeled. (Figure generated using the program MOLSCRIPT [47].)

negative and polar regions of the surface of the molecule. From the electrostatic potential analysis (Fig. 5), it is clear that replacing the Lys13 with a valine as seen in α-elicitins will render this region of the molecule uncharged. Lys13 is located in the middle of the first helix in a position where the Lys→Val substitution would not be expected to cause a conformational change. Therefore, the dramatic alteration of toxicity produced by site directed mutagenesis of this residue is likely to be related to the change in the electrostatic potential of this area.

The calculated solvent-accessible surface shows a large depression centered around the conserved residue Tyr87. The depression, bordered by the Ω loop, the helix α3, the β sheet and the C-terminal helix, is predominantly surrounded by invariant residues except for the three residues Ala2, Asp72 and Lys94. The depression, as depicted in Figure 5a, contains a positively charged region on one side corresponding to Lys94 and a negatively charged region on the other side, corresponding to Asp72. The negative charge of Asp72 is partially neutralized by the charge of the N-terminal amino group. In the less toxic α-elicitins, Lys94 and Ala2 are replaced by threonines and Asp72 is replaced by a glutamic acid. Although the negative charge of residue 72 is maintained as the sidechains of Glu72 and Thr2 are close, steric hindrance between them, in α-elicitins, may affect the conformation of this region. It is clear that the charge-distribution around the depression would be different in α-elicitins from that observed in β-elicitins.

Tyr87, whose side chain plunges into the bottom of the depression, could have a special role in ligand and/or receptor binding. Buried in the core of the molecule, the hydroxyl atom is free from interactions with its neighbours, allowing the phenolic ring to move freely, perhaps opening a deeper cavity. It is noteworthy that tyrosines have been shown to limit the access to active sites in several cases [27]. However, at present there is no evidence of an enzymatic function for the elicitins.

Thus, in addition to the beak-like motif, there are two other regions around residues 13 and 87 for which the charge-distribution is directly correlated to the level of the biological activity of elicitins. In β-elicitins, the surface of these

Figure 3

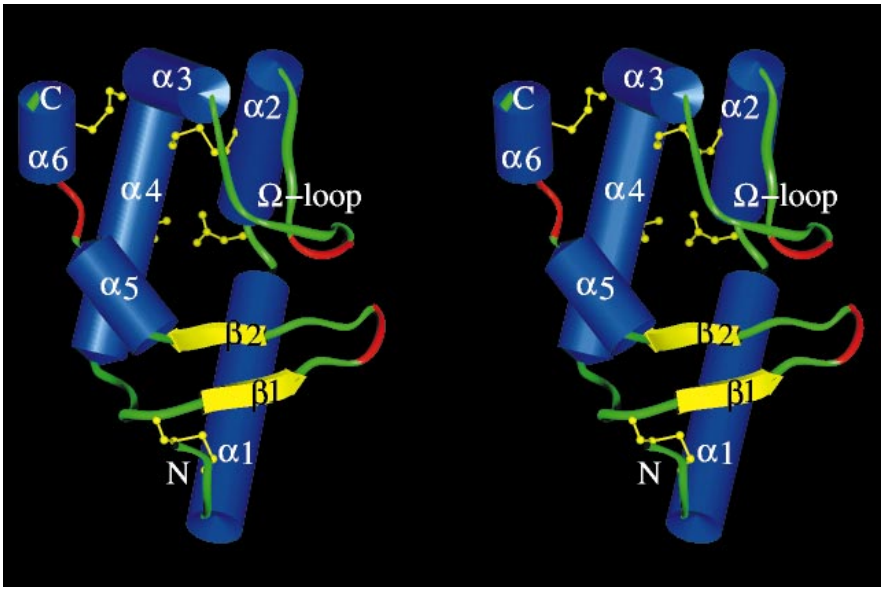

A stereo diagram of the overall fold of CRY. Secondary structure elements are as follows : α1, residues 5–19; α2, 22–31; α3, 44–52; α4, 54–66; β1, 72–74; β2, 81–83; α5, 84–89; and α6, 91–96. The Ω loop which includes residues 33 to 42 connects helices α2 and α3. Helices are shown as blue cylinders and β strands as yellow arrows. Coil elements are represented in green. The two reverse turns and the helical turn that connects helices α5 and α6 are colored red, . The three disulfide bridges (3–71, 27–56, 51–95) and the salt bridge (21–62) are shown in yellow (ball-and-stick). The N and C termini are also marked. (Figure generated using the program Insight II Version 2.2 [Biosym Technologies].)

Figure 4

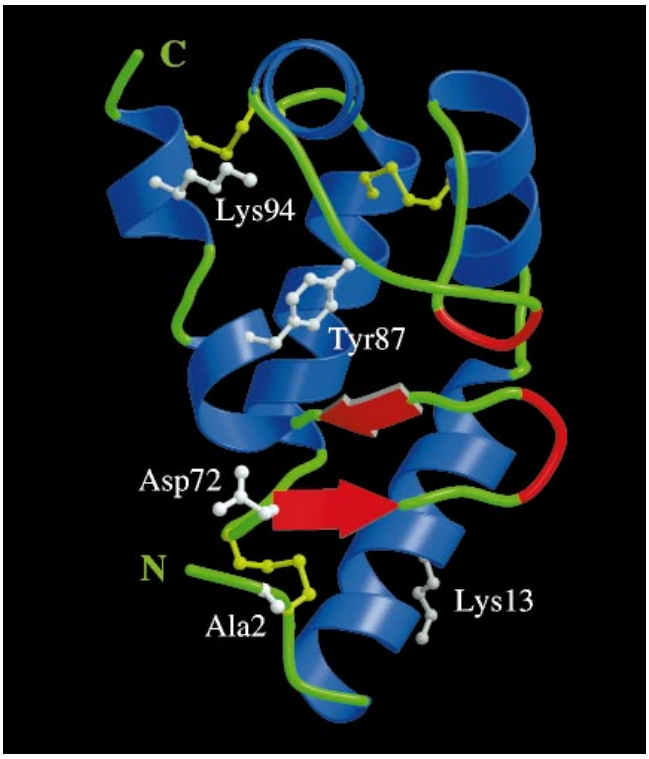

A ribbon diagram of the molecule showing the key residue Lys13 and three putative activity-modulating residues (Ala2, Asp72 and Lys94) in ball-and-stick representation. Helices are shown in blue, β strands and reverse turns in red, and coil loops in green. Disulfide bridges are represented in light green (ball-and-stick). The conserved Tyr87 residue is labeled. (Figure generated using the programs MOLSCRIPT [47] and RASTER3D [48].)

two regions is highly charged. In α-elicitins, the surface is less charged in the depression region around residue 87 and more hydrophobic in the region around residue 13. These two regions of the molecule are good candidates for regions that will prove to be important in receptor-binding.

Molecular environment in the crystal

Although the model shows good geometry and is well-defined by the electron-density map, the overall B factor is rather high (37.3 Å^2). This is consistent with the estimated average temperature factor for the crystal (B_{Wilson} = 38 Å^2). The R_{free} [28] decreased continuously during the course of the refinement, confirming the validity of the results. Two characteristic features of the crystals should be underlined. First, the mosaicity of the crystal was relatively high, both at ambient and cryogenic temperatures. Second, the observed strong thermal diffuse scattering was not lowered by the use of frozen crystals. These two phenomena give rise to the hypothesis of a strong static disorder embedded within the entire crystal lattice. This is consistent with both the unusual high solvent content (66%) and the limited number of contacts between symmetry-related molecules. With an applied cut-off of 3.5 Å and 4.0 Å respectively, direct intermolecular contacts amount to only 6 hydrogen bonds and 63 van der Waals contacts. The lack of intermolecular contacts is therefore in agreement with the observed temperature factor. The analysis of the crystal packing shows half-moon crossing channels, each 43 Å long by 15 Å wide, one parallel to the a, the other to the b axis. A main intermolecular contact is observed in the region around Asn70. A dyad axis is responsible for a hydrogen-bond pair between the amide group of Asn70 and its twofold symmetry-related amide group. Large loose water molecule lattices, which represent

Figure 5

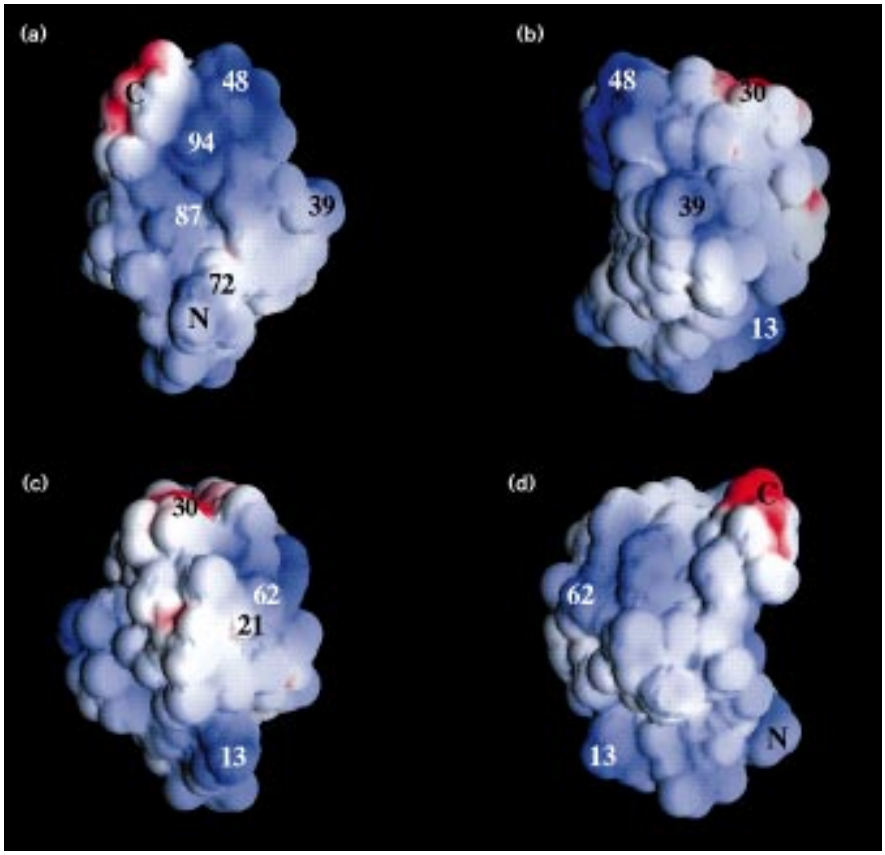

Four views of the electrostatic potential mapped onto the solvent-accessible surface. The views (a)–(d) represent 90° incremental rotations around the vertical axis. The positive potential is shown in blue and the negative potential in red. In agreement with the basic isoelectric point (p*I* ~ 10), the overall surface is mainly positively charged. The few discrete patches of charged residues are labeled. It is noticeable that Lys13 is isolated among a large surface of uncharged variable residues. The depression centred around Tyr87 is depicted in (a), on the left part of (b) and on the right part of (d). The protuberant beak-like motif is clearly visible on the left of (c). The charges of the residues involved in the two salt bridges (1–72 and 21–62) are partially neutralized. (Figure generated using the program GRASP [49].)

a minor contribution to the stabilization of the crystal packing, are observed between symmetry-related molecules, except for helix α1 which is in van der Waals contact with its symmetry-related counterpart. This loose molecular packing may partially explain our difficulty in obtaining useful heavy-atom derivatives. Such a pattern acts as a flow cell where a dialysis phenomenon elutes those elements which are not bound with sufficient affinity. In the case of the platinum derivative, only two residues, Gln26 of helix α2 and Thr54 of helix α4, are involved in anion binding. The weakness of these stabilizing interactions can be correlated with the poor occupancy factor (0.4) and the high temperature factor (60 Å^2) of the anion site.

Analysis of the tyrosine residues

A study of the exposure to the solvent of the strictly conserved tyrosine residues was previously performed by UV difference spectroscopy and the p*K*'s of the phenolic groups were determined [12]. It is interesting to compare these results to the CRY structure reported here. In the earlier study it was shown that Tyr12 is buried in the α-elicitins, and exposed to the solvent in the β-elicitins. In the CRY structure, Tyr12 is indeed exposed to the solvent and the shift of its p*K* towards 11.5 is explained by the hydrogen bond between its hydroxyl and the carbonyl oxygen of Thr74, which links the first helix to the β sheet. Tyr33 is found buried with a hydrogen bond between its hydroxyl and the carbonyl oxygen of Ala40. Consistent with this, Tyr33 was previously observed to be inaccessible to solvent and not titratable. Spectroscopic studies have also shown that Tyr47 is located at the surface of the molecule, as we confirm here. The stacking of the aromatic ring of Tyr47 on Pro42 would partly explain its p*K* shift to over pH 12. The UV data indicate a normal p*K* for Tyr85, which is indeed accessible to the solvent. Tyr87 lies at the bottom of a depression and, although its free hydroxyl is buried into the core of the molecule, its phenolic ring is partly exposed to the solvent. Difference spectroscopy demonstrated that this tyrosine is indeed exposed and its p*K* is only slightly raised (by 0.5 pH unit). In sum, the observed stacking and hydrogen bonds formed by the tyrosines residues explain the fact that the maximal absorbance wavelength of elicitins is 277 nm instead of the 275 nm seen for a free tyrosine. The agreement between the model and the previous data suggests that there is no structural alteration due to crystal packing.

Biological implications

Elicitins are 10 kDa proteins secreted by *Phytophthora* and *Pythium* fungi that are presumably involved in

fungal invasion of plants. They also trigger a defence mechanism in the potential host, however, inducing leaf necrosis and an incompatible hypersensitive-like reaction that leads to resistance against fungal and bacterial plant pathogens. Although many of the cellular events that form the plant's response to elicitins have been described, the molecular mechanism of elicitins action is presently unknown. Potential high-affinity binding sites for β-cryptogein (CRY), an elicitin secreted by *Phytophthora cryptogea* [14], have been detected in the plasma membrane from tobacco cells.

The present study of the crystal structure of CRY at 2.2 Å resolution provides the first structural information on the elicitins. The polypeptide chain fold is a novel folding type. The structure reveals a new beak-like motif that is highly conserved in all elicitins. This motif is likely to be a major recognition site for a putative receptor and/or ligand. Two other regions appear to be involved in receptor or ligand binding, and their composition correlates with the level of necrotic-activity.

The knowledge of the elicitin structure will allow the engineering of non-toxic elicitins that can elicit plant defences without creating damage. It now becomes possible to imagine that elicitins could be used as the basis of a general method to protect plants against a range of phytopathogenic microorganisms. One may hope to design an elicitin gene modified for its ability to successfully induce plant resistance against pathogens and transfer it to diverse plant genomes. Knowledge of the necrotic motifs, on the other hand, may allow the production of new herbicides. Both transgenic plants and toxic chemicals would be helpful not only to support progress in the understanding of the plant defence systems, but also to provide agriculture with new protective means to prevent pathogens from causing crop losses, without damaging the environment.

Materials and methods

Crystallization and heavy-atom derivatives search

CRY was crystallized in concentrated sodium chloride as previously described by Guilloteau *et al.* [16]. Use of macroseeding procedures made it possible to systematically grow well shaped and sufficiently large crystals overnight through the pH range 4.0 to 10.0, while eliminating twinning which is frequent in this crystalline form. A supersaturated solution was prepared by the hanging drop vapor diffusion method from a stock solution of 75 mg ml^{-1} protein, 0.02% NaN_3 and 10 mM NaCl stock solution mixed with reservoir solution in proportion to a 1/3:2/3 or 1/4:3/4 volume ratio. Four microliters of this mixture were deposited on a siliconized coverslip and left to equilibrate with the 4.85 M NaCl precipitation buffer. The buffer used was 50 mM sodium acetate pH 4.0, 50 mM Tris-HCl pH 7.50 or 50 mM 3-[cyclohexylamino]-1-propanesulfonic acid (CAPS) pH 10.0. Washed microsized crystals were then seeded into the resultant pre-equilibrated solution and grew within a few hours. The crystals belong to tetragonal space group $P4_122$ with unit cell parameters a = b = 46.5 Å, c = 134.9 Å, with one molecule per asymmetric unit. High resolution data were collected at 4 °C with synchrotron radiation (λ = 0.9 Å) to a minimum Bragg spacing of 2.2 Å at station DW32 of the LURE (Orsay, France) using a wiggler beam line. The diffraction images were indexed and integrated using MOSFLM [29]. The complete intensity set was scaled, merged, reduced to unique reflections and truncated with programs from the CCP4 suite [30]. No significant degradation was observed after X-ray exposure. This has allowed us to record a 97.2% complete data set from a single crystal for which all data were usable (< I/sigI > = 4.6 for the last resolution shell).

In the course of the extensive heavy-atom derivatives search, only a tetrachloroplatinate (K_2PtCl_4) derivative was obtained that yielded to a poor phasing power. In addition to the loose crystal packing, this may be related to the absence of four types of amino acids in the sequence of CRY (there are no His, Glu, Arg or Trp residues) and to the high ionic strength in which crystals are obtained. More favourable crystallization precipitating reagents led to a new crystalline form in PEG8000 19% (w/v), 200 mM LiCl, 0.02% NaN_3 and 100 mM Tris-HCl pH 7.0. Data were collected using a Xentronics imaging detector and indexed by XDS [31] in a triclinic space group P1 (a = 69.1 Å, b = 76.4 Å, c = 87.2 Å, α = 90° 2, β = 110° 3, γ = 95° 6). The self-rotation function showed a 422 pseudosymmetry and precession photographs failed to find any crystallographic symmetry. The calculated specific protein volume V_m = 2.6 Å^3 Da^{-1} corresponding to a solvent content of 53% was consistent with 16 molecules in the asymmetric unit. The difficulties associated to a triclinic space group with high pseudosymmetry led us to leave this crystalline form and concentrate our efforts on the platinum derivative.

Figure 6

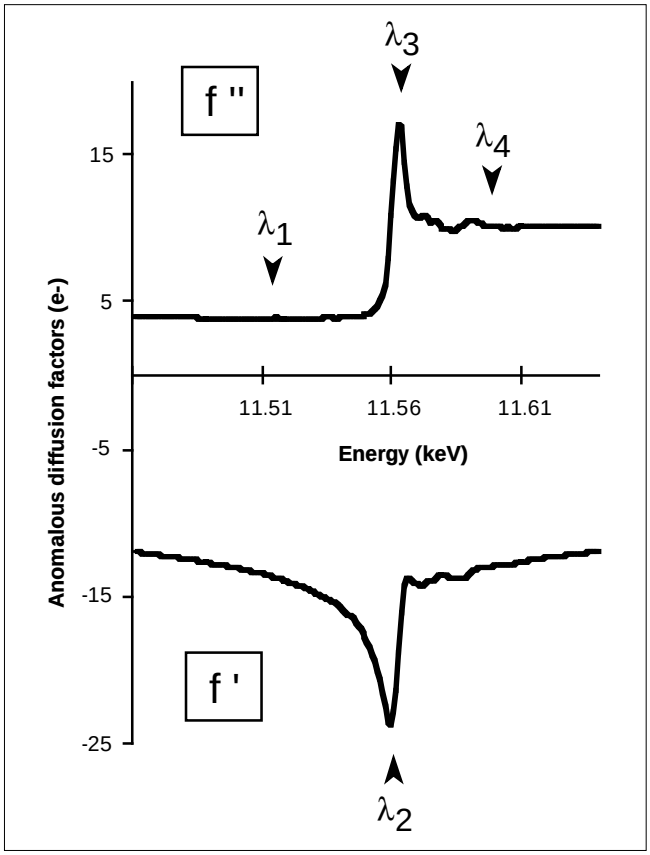

The energy dependence of the anomalous scattering factors f′ and f′′ in the vicinity of Pt L_{III} absorption edge as derived from the fluorescence spectrum recorded on a Pt-CRY crystal according to the procedure described by Hendrickson *et al.* [50]. The four working wavelengths are noted: edge (λ2), peak (λ3) and two remote points (λ1 and λ4).

Table 3

Relative peak heights in anomalous and isomorphous Patterson syntheses.

Harker unique vectors			Isomorphous* difference (12–3.5 Å)	MAD dataset*			
u	v	w		Anomalous Bijvoet differences (8–3 Å)	Anomalous dispersive differences (10–4 Å)	Isomorphous differences (12–3.5 Å)	Anomalous differences (10–3 Å)
2x	2y	1/2	3.64 (6)	4.97 (5)	3.30 (9)	6.1 (4)	7.4 (3)
x + y	y – x	3/4	5.44 (3)	5.59 (4)	5.32 (3)	7.7 (2)	7.2 (4)
2x	0	2z	2.90 (11)	2.90 (24)	3.23 (10)	5.3 (6)	5.0 (8)
0	2y	2z + 1/2	2.96 (9)	3.62 (10)	2.18 (27)	2.8 (29)	3.1 (17)
x – y	y – x	2z + 1/4	9.33 (2)	11.05 (2)	8.06 (2)	14.6 (1)	15.2 (1)
x + y	x + y	2z + 3/4	2.51 (16)	4.31 (7)	2.75 (12)	4.0 (12)	5.6 (7)

Unique Harker vectors of the unique Pt heavy-atom site are shown for the MAD dataset. They were calculated using programs from the CCP4 suite [30] or the routine MADMRG of the program HEAVYv4 [51], which reduces MAD data to isomorphous plus anomalous differences. The signal-to-noise ratio of these Patterson syntheses was optimized by screening the resolution range and the cut-off conditions. The most informative differences expected for each kind of signal, as calculated using programs from the CCP4 suite, were chosen: $|F_{Native2}(h) - F_{\lambda 1}(h)|$ (isomorphous differences), $|F_{\lambda 3}(h^+) - F_{\lambda 3}(h^-)|$ (anomalous Bijvoet differences) and $|F_{\lambda 2}(h) - F_{\lambda 1}(h)|$ (anomalous dispersive differences). The program HEAVYv4 produced only two kinds of differences, isomorphous and anomalous, and enhanced the signal-to-noise ratio of the Patterson map. *Peak heights are given as root mean squares and their sorting numbers are shown in parentheses.

MAD experiment

MAD diffraction data were collected at four wavelengths on D2AM beam line at the European Synchrotron Radiation Facility (ESRF) in Grenoble (France). Heavy-atom soaking was done by mixing 2.7 µl of a K_2PtCl_4 stock solution to a drop surrounding a crystal. Because there is no known stabilizing solution, the crystal was withdrawn and immediately transferred to and preserved in a previously removed crystal drop in order to roughly wash it from concentrated platinum (50 mM). An equal amount of a cryoprotectant solution of 30 % (w/v) glycerol in 4.85 M NaCl, 50 mM Tris-HCl was then added a few seconds before the crystal was harvested with a fine dental-floss loop and flash-cooled to 100 K [32] in a stream of nitrogen gas from a Cryostream (Oxford Cryosystems, Oxford, UK). The X-ray optics were set up to optimize the platinum L_{III} absorption edge signal by measuring the fluorescence of platinum foil using a photomultiplier placed at a right angle to the beam, in its polarization plane. A similar fluorescence spectrum, recorded with the frozen crystal, was used to select the wavelengths in the absorption edge (λ_2 = 1.0726 Å, maximum of |f′|), at the peak (λ_3 = 1.0722 Å, maximum of f″) and at two remote points (λ_1 = 1.0766 Å, λ_4 = 1.0696 Å) on both sides from the peak as shown in Figure 6. The crystal was approximately aligned along the elongation axis c* so that Bijvoet pairs could be almost simultaneously recorded. Oscillation diffraction patterns were recorded on a detector designed at the ESRF from a Thomson image intensifier coupled to a Princeton CCD camera [33]. The speed of the CCD detector combined with the brightness of the beam line have allowed the complete data collection (420 frames) in less than six hours. Reflections were indexed using profile-fitting as implemented in a local version of XDS [34] modified by W. Kabsch and intensities were scaled at each wavelength. Concomitant image scaling at each wavelength was also performed. The CCP4 suite of programs was then used to merge and to process these intensities; anomalous differences were calculated by the CCP4 program AGROVATA. A native data set was collected at the same time on a frozen crystal (a = b = 46.4 Å, c = 132.8 Å). Data statistics for the whole data reduction procedure are presented in Table 1.

Maximum-likelihood parameter refinement and phasing

The MAD data sets were subjected to an anisotropic scaling using SCALEIT (CCP4) with the λ_1 wavelength as a reference. The anomalous components of each reflection were extracted to form either Bijvoet differences ($F\lambda_i(h^+) - F\lambda_i(h^-)$) at each wavelength *i* or dispersive differences ($F\lambda_i(h) - F\lambda_j(h)$) at pairs (*i*, *j*) of wavelengths and were input as coefficients to calculate Patterson map syntheses. Table 3 presents the results obtained from the inspection of Harker sections of these Patterson maps. They were calculated for the best expected signals, on the one hand with Bijvoet differences at the peak absorption, and on the other hand with dispersive differences between the 'edge' and 'remote' wavelengths. Automatic interpretation of heavy-atom Harker and cross vector positions with RSPS [35] was coherent with a single platinum site. No additional less occupied sites were later found.

The refinement of parameters for heavy-atoms, relative scales between data sets, and lack-of-isomorphism (l.o.i.), was carried out using SHARP (for Statistical Heavy-Atom Refinement and Phasing) [18]. The main advantages of SHARP over existing programs are: a full two-dimensional integration (i.e. integration over both modules and phase of the native structure factor) to compute the likelihood function; a genuine likelihood maximization (rather than phase-integrated least-squares), which enables the parameters of the error model to be refined along with all the other conventional parameters; and a hierarchical data structure that enables any type of dataset (MIR, MAD, or both combined) to be described. The native dataset, if present, is described as any other derivative, but with no heavy atom specified. In this way, the l.o.i. parameters are kept at zero values for the native or any derivative dataset which is therefore set as the reference for isomorphism. User-friendliness, online documentation and graphics are provided through a GUI (Graphical User Interface). Owing to the new radial integration (two-dimensional integration) mentioned above, there is no obligation in SHARP to define a 'native' dataset.

In the present case, the MAD experiment was described straightforwardly as derivative data at four different wavelengths, the only parameters varying being f′, f″, the scale parameters and the l.o.i. parameters. In this case, l.o.i. does not describe physical lack-of-isomorphism, but the effect of an inaccurate heavy-atom model, and of inadequacies in the estimation of experimental standard deviations. Since the single Pt site of low occupancy had a low phasing power, it was necessary to use a solvent-flattening procedure to produce interpretable electron-density maps, and thus to evaluate the success of the phasing procedure.

The electron-density maps obtained using the phase probability distributions produced by SHARP, after solvent-flattening by program SOLOMON [36] using the MAD dataset only, were far more interpretable than those obtained from phase distributions produced by other programs. Addition of

Table 4

MAD phasing statistics for CRY-Pt crystal.

	Observed MAD difference ratios*				Anomalous scattering factors†	
	remote1	edge	peak	remote2	f′ (e^-)	f″ (e^-)
Remote1 (λ1)	0.027	0.016	0.014	0.013	–13.7	9.7
Edge (λ2)		0.030	0.015	0.015	–20.2	14.2
Peak (λ3)			0.034	0.011	–17.3	19.2
Remote2 (λ4)				0.031	–13.7	17.1
R_{iso} (%)‡	11.5					
R_{disp} (%)§		1.4	1.3	1.0		

*Observed MAD difference ratios rms(△|F|)/rms(|F|) [50], where △|F| is either the Bijvoet difference at one wavelength (diagonal elements) or the dispersive difference between two wavelengths (off-diagonal elements). These statistics are calculated on fully observed reflections ($F(h^+)$ and $F(h^-)$ at all four wavelengths), e.g. 2101 reflections out of 3286 between 32.6 and 2.9 Å. †Values of anomalous scattering factors as refined by SHARP [18], that were used for phasing.
‡$R_{iso} = \Sigma_h |F_{\lambda 1}(h) - F_{Native2}(h)| / \Sigma_h |F_{Native2}(h)|$
§$R_{disp} = \Sigma_h |F_{\lambda i}(h) - F_{\lambda 1}(h)| / \Sigma_h |F_{\lambda 1}(h)|$ is similar to R_{iso} with λ1 acting like the reference set. Mean figure of merit (FOM) = 0.46 including reflections with FOM = 0; Pt occupancy factor = 0.42.

a native dataset (Native2, Table 1) in the calculation has been instrumental in phasing the 3286 reflections with an average figure of merit of 0.46 over the resolution shell 32.0–2.9 Å. Solvent-flattening iterations performed with the SOLOMON program described above raised the figure of merit to 0.81 (Table 4). This resulted in a continuous and completely interpretable electron-density map.

Model building and refinement

Two uncertainties were associated with the crystals: the solvent content and the space group ($P4_122$ or its enantiomorph $P4_322$). The equilibrium gradient method [37] gave inconclusive results for the number of molecules in the asymmetric unit. Self-rotation maps were free of additional pseudo twofold axis and were consistent with one molecule per asymmetric unit, although this case corresponds to an unusually high V_m value of 3.7 $Å^3 Da^{-1}$ [38]. A perfectly interpretable map has been obtained using this hypothesis (66% solvent content), confirming that the asymmetric unit contains one CRY molecule. The space group was clearly defined as $P4_122$ by the right-handedness of α helices.

The 2.9 Å MAD-phased electron-density map was skeletonized using BONES [39] allowing a fast Cα tracing using the XFIT graphic tools of the program XTALVIEW [40]. The model building was made easier by viewing the symmetrical traces of the backbone after transformation into a PDB type file using the program MAPMAN from the RAVE package [41]. The total lack of ambiguity combined with the perfect electron-density continuity have allowed the rapid construction of the 98 amino acids corresponding to the whole CRY sequence with TURBO-FRODO [42]. The identification of the three disulfide bridges was helpful in connecting the secondary structural elements, especially Cys3–Cys71 and Cys51–Cys95 which were useful in the recognition of the N- and C-terminal helices. The starting model showed no residues in the disallowed region of the Ramachandran plot. The first round of refinement by energy minimization using X-PLOR [43] allowed the crystallographic R factor to drop from 46.4% to 30.5% in the range from 10.0 to 2.9 Å resolution. After a few energy minimization and model rebuilding steps we decided to continue the refinement process using high resolution data (Native1, Table 1). Because of the weak non-isomorphism induced by the freezing process the model was refitted into the 4° C unit cell using the molecular replacement program AMoRe [44]. During the course of the refinement, minor modifications were made to the initial model, such as the flipping of Pro76 and Ser34 or the building of the last C-terminal residue for which the corresponding initial MAD electron-density map was missing. A series of simulated annealing omit maps excluding atoms located in a 8 Å sphere surrounding the doubtful residues have allowed them to be corrected. To refine the model, a slow-cool procedure was used with the heat stage being performed at 3000 K. After each refinement cycle the model was checked against $3F_o–2F_c$ maps and manually adjusted to improve the geometry. Water molecules were added very early on because some of them were already clearly visible on the 3 Å resolution MAD map. Both a clear density bubble within a 2.5 σ contoured $F_o–F_c$ Fourier difference map and connections less than 3.4 Å to a possible hydrogen donor or acceptor were strictly required to assign a peak to a water molecule. The crystallographic R factor for the final CRY model comprising 66 water molecules is 21.8% between 7 Å and 2.2 Å. A subset of 7.5% of all reflections was excluded from the refinement and was used to calculate a R_{free} = 27.9%. Root mean square (rms) deviations from the stereochemical standards bond lengths and bond angles are 0.013 Å and 1.50° respectively. The stereochemistry of the model was analysed using PROCHECK [45]. The secondary structures were assigned by the criteria of Kabsch and Sander [46], as implemented in PROCHECK.

Accession numbers

The atomic coordinates of β-cryptogein have been deposited in the Brookhaven Protein Data Bank (entry code 1BEO).

Acknowledgements

The authors gratefully acknowledge Michel Roth for having provided access to the D2AM beamline of ESRF (Grenoble, France), Jean-Luc Ferrer and Eric Fanchon for help and advice with MAD data collection, Valérie Perez for fungus culture and CRY purification, Michael O'Donohue for critical comments on this manuscript, the staff of LURE (Orsay, France) for making station DW32 available to us and Fred Saul for assistance in data collection.

References

1. Dixon, R.A. & Lamb, C.J. (1990). Molecular communication in interactions between plants and microbial pathogens. *Annu. Rev. Plant Physiol. Plant Mol. Biol.* **41**, 339–367.
2. Ricci, P., *et al.*, & Pernollet, J.-C. (1989). Structure and activity of proteins from pathogenic fungi *Phytophthora* eliciting necrosis and acquired resistance in tobacco. *Eur. J. Biochem.* **183**, 555–563.
3. Kamoun, S., Young, M., Glascock, C.B. & Tyler, B.M. (1993). Extracellular protein elicitors from *Phytophthora*: host-specificity and induction of resistance to bacterial and fungal phytopathogens. *Mol. Plant Microbe Interact.* **6**, 15–25.
4. Kamoun, S., Young, M., Förster, H., Coffey, M.D. & Tyler, B.M. (1994). Potential role of elicitins in the interaction between *Phytophthora* species and tobacco. *Appl. Environ. Microbiol.* **60**, 1593–1598.
5. Pernollet, J.-C., Sallantin, M., Sallé-Tourne, M. & Huet, J.-C. (1993). Elicitin isoforms from seven *Phytophthora* species: comparison of their physico-chemical properties and toxicity to tobacco and other plant species. *Physiol. Mol. Plant Pathol.* **42**, 53–67.

6. Huet, J.-C., Le Caer, J.-P., Nespoulous, C. & Pernollet, J.-C. (1995). The relationships between the toxicity and the primary and secondary structures of elicitin-like protein elicitors secreted by the phytopathogenic fungus *Pythium vexans*. *Mol. Plant Microbe Interact.* 8, 302–310.
7. Huet, J.-C. & Pernollet, J.-C. (1989). Amino acid sequence of cinnamomin, a new member of the elicitin family, and its comparison to cryptogein and capsicein. *FEBS Lett.* 257, 302–306.
8. Nespoulous, C., Huet, J.-C. & Pernollet, J.-C. (1992). Structure–function relationships of α and β elicitins. Signal proteins involved in the plant–*Phytophthora* interaction. *Planta* 186, 551–557.
9. Huet, J.-C. & Pernollet, J.-C. (1993). Sequences of acidic and basic elicitin isoforms secreted by *Phytophthora megasperma megasperma*. *Phytochemistry* 33, 797–805.
10. Huet, J.-C., Mansion, M. & Pernollet, J.-C. (1993). Amino acid sequence of the a elicitin secreted by *Phytophthora cactorum*. *Phytochemistry* 34, 1261–1264.
11. Huet, J.-C., Sallé-Tourne, M. & Pernollet, J.-C. (1994). Amino acid sequence and toxicity of the a elicitin co-secreted with ubiquitin by *Phytophthora infestans*. *Mol. Plant Microbe Interact.* 7, 302–304.
12. Nespoulous, C. & Pernollet, J.-C. (1994). Local structural differences between α and β elicitins shown by CD and ultraviolet difference spectroscopy. *Int. J. Pept. Protein Res.* 43, 154–159.
13. O'Donohue, M.J., Gousseau, H., Huet, J.-C., Sallantin, M., Tepfer, D.A. & Pernollet, J.-C. (1995). Chemical synthesis, expression and mutagenesis of a gene coding for β-cryptogein, a *Phytophthora cryptogea* elicitin. *Plant Mol. Biol.* 27, 577–586.
14. Wendehenne, D., Binet, M.-N., Blein, J.-P., Ricci, P. & Pugin, A. (1995). Evidence for specific, high-affinity binding sites for a proteinaceous elicitor in tobacco plasma membrane. *FEBS Lett.* 374, 203–207.
15. O'Donohue, M., Boissy, G., Huet, J.C., Nespoulous, C., Brunie, S. & Pernollet, J.C. (1996) Overexpression in *Pichia pastoris* and crystallization of an elicitor protein secreted by the phytopathogenic fungus *Phytophthora cryptogea*. *Protein Expr. Purif.* 8, 254–261.
16. Guilloteau, J.-P., Nespoulous, C., Huet, J.-C., Beauvais, F., Pernollet, J.-C. & Brunie, S. (1993). Crystallization and preliminary X-ray diffraction studies of β-cryptogein, a toxic elicitin secreted by the phytopathogenic fungus *Phytophthora cryptogea*. *J. Mol. Biol.* 229, 564–565.
17. Newman, M., Strzelecka, T., Dorner, L.F., Schildkraut, I. & Aggarwal, A.K. (1994). Structure of restriction endonuclease *Bam*HI phased at 1.95 Å resolution by MAD analysis. *Structure* 2, 439–452.
18. de La Fortelle, E. & Bricogne, G. (1996). Maximum likelihood heavy-atom parameter refinement in the MIR and MAD methods. In *Methods in Enzymology*. (Carter, C.W. & Sweet, R.M., eds), pp. 472–294, Academic Press, UK.
19. Ramachandran, G.N. & Sasisekharan, V. (1968). Conformation of polypeptides and proteins. *Adv. Protein Chem.* 23, 283–438.
20. Holm, L. & Sander, C. (1993). Protein structure comparison by alignment of distance matrices. *J. Mol. Biol.* 233, 123–138.
21. Kleywegt, G.J. & Jones, T.A. (1995). Where freedom is given, liberties are taken. *Structure* 3, 535–540.
22. Gibrat, J.-F., Madej, T. & Bryant, S.H. (1996). Surprising similarities in structure comparison. *Curr. Opin. Struct. Biol.* 6, 377–385.
23. Bernstein, F.C., *et al.*, & Tasumi, M. (1977). The Protein Data Bank: a computer-based archival file for macromolecular structures. *J. Mol. Biol.* 112, 535–542.
24. Bouaziz, S., Van Heijenoort, C., Guittet, E., Huet, J.-C. & Pernollet, J.-C. (1994). Resonance assignment, cysteine-pairing elucidation and secondary-structure determination of capsicein, an α-elicitin, by three-dimensional 1H NMR. *Eur. J. Biochem.* 220, 427–438.
25. Leszczynski, J.F & Rose, G.D. (1986). Loops in globular proteins: a novel category of secondary structure. *Science* 234, 849–855.
26. Fetrow, J.S. (1995). Omega loops : nonregular secondary structures significant in protein function and stability. *FASEB J.* 9, 708–717.
27. Benson, T.E., Walsh, C.T. & Hogle, J.M. (1996). The structure of the substrate-free form of MurB, an essential enzyme for the synthesis of bacterial cell walls. *Structure* 4, 47–54.
28. Brünger, A.T. (1992). Free R value: a novel statistical quantity for assessing the accuracy of crystal structure refinement. *Nature* 355, 472–475.
29. Leslie, A.G.W. (1992). Recent changes to the MOSFLM package for processing film and image plate data. In *Joint CCP4 and ESF-EACBM Newsletter on Protein Crystallography, No. 26*. SERC Daresbury Laboratory, Warrington, UK.
30. Collaborative Computational Project, No. 4. (1994). The CCP4 Suite: programs for protein crystallography. *Acta Cryst. D* 50, 760–763.
31. Kabsch, W. (1993). Automatic processing of rotation diffraction data from crystals of initially unknown symmetry and cell constants. *J. Appl. Cryst.* 26, 795–800.
32. Rodgers, D.W. (1994). Cryocrystallography. *Structure* 2, 1135–1140.
33. Moy, J.-P. (1994). A 200 mm input field, 5–80 keV detector based on an X-ray image intensifier and CCD camera. *Nucl. Instrum. Meth. Phys. Res. A* 348, 641–644.
34. Kabsch, W. (1988). Evaluation of single crystal X-ray diffraction data from a position-sensitive detector. *J. Appl. Cryst.* 21, 916–924.
35. Knight, S. (1989). Ribulose 1,5-bisphosphate carboxylase/oxygenase - A structural study. Thesis, Swedish University of Agricultural Sciences, Uppsala, Sweden.
36. Abrahams, J.P. & Leslie, A.G.W. (1996). Methods used in the structural determination of bovine mitochondrial F_1 ATPase. *Acta Cryst. D* 52, 30–42.
37. Westbrook, E.M. (1985). Crystal density measurements using aqueous ficoll solutions. *Methods Enzymol.* 114, 187–196.
38. Matthews, B.W. (1968). Solvent content of protein crystals. *J. Mol. Biol.* 33, 491–497.
39. Jones, T.A., Zou, J.Y., Cowan, S.W. & Kjeldgaard, M. (1991). Improved methods for building protein models in electron density maps and the location of errors in these models. *Acta Cryst. A* 47, 110–119.
40. McRee, D.E. (1993). Practical protein crystallography. Academic Press, San Diego, CA, USA.
41. Kleywegt, G.J. & Jones, T.A. (1994). Halloween... Masks and Bones. In *From first map to final model*. (Bailey, S., Hubbard, R. & Waller, D., eds), pp. 59–66, SERC Daresbury Laboratory, Warrington, UK.
42. Roussel, A. & Cambillau, C. (1992). TURBO-FRODO. Biographics, LCCMB, Marseille, France.
43. Brünger, A.T., Kuriyan, J. & Karplus, M. (1987). Crystallographic R factor refinement by molecular dynamics. *Science* 235, 458–460.
44. Navaza, J. (1994). AMoRe: an automated package for molecular replacement. *Acta Cryst. A* 50, 157–163.
45. Laskowski, R.A., MacArthur, M.W, Moss, D.S. & Thornton, J.M. (1993). PROCHECK: a program to check the stereochemical quality of protein structures. *J. Appl. Cryst.* 26, 283–291.
46. Kabsch, W. & Sander, C. (1983). Dictionary of protein secondary structures : pattern recognition of hydrogen-bonded and geometrical features. *Biopolymers* 22, 2577–2637.
47. Kraulis, P.J. (1991). MOLSCRIPT: a program to produce both detailed and schematic plots of protein structure. *J. Appl. Cryst.* 24, 946–950.
48. Merritt, E.A. & Murphy, M.E.P. (1994). Raster3D Version 2.0: a program for photorealistic molecular graphics. *Acta Cryst. D* 50, 869–873.
49. Nicholls, A., Bharadwaj, R. & Honig, B. (1993). GRASP: a graphical representation and analysis of surface properties. *Biophys. J.* 64, A166.
50. Hendrickson, W.A., Smith, J.L., Phizackerley, R.P. & Merritt, E.A. (1988). Crystallographic structure analysis of lamprey hemoglobin from anomalous dispersion of synchrotron radiation. *Proteins* 4, 77–88.
51. Terwilliger, T.C. (1994). MAD phasing: treatment of dispersive differences as isomorphous replacement information. *Acta Cryst. D* 50, 17–23.